

# Extracting double-quantum coherence in two-dimensional electronic spectroscopy under pump-probe geometry

Mao-Rui Cai,<sup>1</sup> Xue Zhang,<sup>1</sup> Zi-Qian Cheng,<sup>1</sup> Teng-Fei Yan,<sup>2</sup> and Hui Dong<sup>1,\*</sup>

<sup>1</sup>*Graduate School of China Academy of Engineering Physics, Beijing 100193, China*

<sup>2</sup>*School of Microelectronics, shanghai university, Shanghai 200444, China*

Two-dimensional electronic spectroscopy (2DES) can be implemented with different geometries, e.g., BOXCARS, collinear and pump-probe geometries. The pump-probe geometry has its advantage of overlapping only two beams and reducing phase cycling steps. However, its applications are typically limited to observe the dynamics with single-quantum coherence and population, leaving the challenge to measure the dynamics of the double-quantum (2Q) coherence, which reflects the many-body interactions. We propose an experimental technique in 2DES under pump-probe geometry with a designed pulse sequence and the signal processing method to extract 2Q coherence. In the designed pulse sequence with the probe pulse arriving earlier than pump pulses, our measured signal includes the 2Q signal as well as the zero-quantum (0Q) signal. With phase cycling and the data processing using causality enforcement, we extract the 2Q signal. The proposal is demonstrated with the rubidium atoms. And we observe the collective resonances of two-body dipole-dipole interactions of both  $D_1$  and  $D_2$  lines.

## I. INTRODUCTION

Two-dimensional (2D) spectroscopy [1–4], inspired by multi-dimensional nuclear magnetic resonance, stands as a powerful nonlinear spectroscopic approach [1] for investigating the couplings, structure, and dynamics of systems in both gaseous [5–8] and condensed phases [9, 10]. With advancements in ultrashort pulsed-laser technology, this method has achieved notable success, particularly in the infrared (IR) [11–14] and visible regions [15–17], and has been further extended into the ultraviolet (UV) [18, 19], terahertz (THz) [20, 21], and hybrid regions [22–25].

2D spectroscopy is primarily employed for the study of third-order responses, and also has been developed to explore signals of higher orders. The experimental realization of third-order 2D spectroscopy typically involves a sequence of four laser pulses with a well-defined time ordering [4, 26]. Among these pulses, three are employed to induce the third-order nonlinear response [1] of a sample, while the fourth serves as an auxiliary pulse for detection purposes. Specifically, by interacting with the sample, the first pulse generates a coherence upon arrival. Subsequently, the second pulse transforms the coherence into either a double-quantum (2Q) [27] or zero-quantum (0Q) coherence, which is then converted into another coherence by the third pulse. In the context of heterodyne detection, the third-order nonlinear signal generated by the final coherence is detected by treating the auxiliary pulse as the local oscillator (LO) [28–30]. Alternatively, in fluorescence detection, the auxiliary pulse converts the coherence into an excited population and the fluorescence signal is detected directly in time domain [5].

Third-order 2D spectroscopy is usually implemented with different geometries, e.g., BOXCARS [28, 29],

collinear [5, 7, 21], and pump-probe geometries [30–33]. Depending on which intervals between the three excitation pulses are scanned and Fourier transformed, third-order 2D spectroscopy is denoted as one-quantum (1Q) 2D spectroscopy, or 2Q (or 0Q) 2D spectroscopy [27, 34, 35]. Third-order 2Q 2D spectroscopy characterizes the 2Q coherence between the ground and a doubly excited level, which either naturally exists within an individual or originates from many-body interactions [6, 27, 29]. In experiments of third-order 2Q 2D spectroscopy, the BOXCARS [6, 29] and collinear [7] geometries have been widely utilized and developed [36, 37]. Whereas, the pump-probe geometry, though alleviates the challenges of implementing 2D spectroscopy, is barely reported in third-order 2Q studies, limited by its phase matching condition. Attempt was tried to measure the fifth-order 2Q coherence using 2D spectroscopy under pump-probe geometry [38]. Yet the associated signals are generally much weaker compared to the third-order ones.

Recently, Farrell and Zanni [39] have realized measuring third-order 2Q coherence using 2D IR spectroscopy under pump-probe geometry with a permuted-pump-probe pulse sequence. In their sequence, the probe pulse arrives at the sample secondly (or firstly) [39, 40], which is different from the traditional pump-probe sequence [30–33] with the probe pulse arriving lastly. With the permuted-pump-probe pulse sequence, 2Q and 0Q signals have the same phase matching direction and thus will be simultaneously detected. By retrieving the imaginary part of the third-order response from the real valued signal using a time-domain Kramers-Kronig inversion [3, 31, 39], 2Q and 0Q coherences are separated at opposite quadrants  $(+\omega_1, +\omega_3)$  and  $(-\omega_1, +\omega_3)$  on a common spectra.

In this paper, we extend this detection technique to 2Q 2D electronic spectroscopy (2Q 2DES) under pump-probe geometry by detecting the third-order 2Q coherence in rubidium atoms [34] with additional data processing method and phase cycling. Our theoretical analysis

\* [hdong@gscap.ac.cn](mailto:hdong@gscap.ac.cn)

and experimental methodology rely on utilizing a pulse shaper to transform a single pump pulse into two distinct pump pulses [13, 41]. The interval and phases of these two pump pulses are controlled through the acousto-optic modulator (AOM) in the pulse shaper. We find that the effective oscillation frequencies of 2Q and 0Q coherences during the scanned interval  $T$  are not always opposite, i.e., the 2Q and 0Q coherences could potentially reside at the same quadrant on 2D spectrum. Therefore, we employ the phase cycling scheme  $(0, 0)$  and  $(0, \pi/2)$  of the two pump pulses [31] to effectively separate the 2Q and 0Q coherences into different spectra, allowing for their independent analysis without mutual interference. In addition, to the best of our knowledge, we have firstly demonstrated the simultaneous observation of 2Q coherences both for an individual rubidium atom [34] and for collective resonances arising from dipole-dipole interactions associated with both two  $D$  lines [42] of rubidium atoms.

## II. DETECTING DOUBLE-QUANTUM COHERENCE

### A. Phase matching condition and pulse sequence

Two-dimensional spectroscopy under pump-probe geometry is a special partial-collinear 2D spectroscopy [30, 32], where two (pump) pulses are collinear and the third (probe) pulse takes a non-collinear direction with respect to these two. Such a 2D spectroscopy has gained exclusive successes in studying the coherent phenomena in several systems in recent ten years [14, 43–46]. The traditional pulse sequence of the 1Q 2D spectroscopy is shown in Fig. 1(a). In this sequence, the two pump pulses arrive at the sample before the probe pulse, and the intervals between the three pulses are denoted as  $\tau$  and  $T$ .

Under the pump-probe geometry, the third-order signals induced by the three different pulses are typically heterodynely detected in the frequency domain  $\omega_t$  along phase matching direction  $\vec{k}_s = \pm \vec{k}_1 \mp \vec{k}_1' + \vec{k}_2 = \vec{k}_2$ , where we denote  $\vec{k}_1$  and  $\vec{k}_1'$  ( $\vec{k}_1 = \vec{k}_1'$ ) as the wave vectors of the two pump pulses, and  $\vec{k}_2$  as the wave vector of the probe pulse. Under this geometry, the probe pulse not only interacts with the investigated sample but also serves as the LO [41]. In order to fulfill the phase matching condition above, one of the two pump pulses must have its conjugated field interacting with the sample. An example of the detectable pathway for 1Q 2D spectroscopy is shown in Fig. 2(a), where the first pump pulse induces a coherence  $\rho_{eg}$  and the conjugated field of the second pump pulse converts the  $\rho_{eg}$  into a population state (0Q coherence)  $\rho_{ee}$ .

To study the 2Q coherence during  $T$ , the first two pulses are both used to induce a 2Q coherence (i.e.,  $\rho_{gg} \rightarrow \rho_{eg} \rightarrow \rho_{fg}$ ) while the conjugated fields of the third pulse converts the 2Q coherence  $\rho_{fg}$  into a coherence  $\rho_{eg}$ , as shown by the pathway Fig. 2(b). Here, we

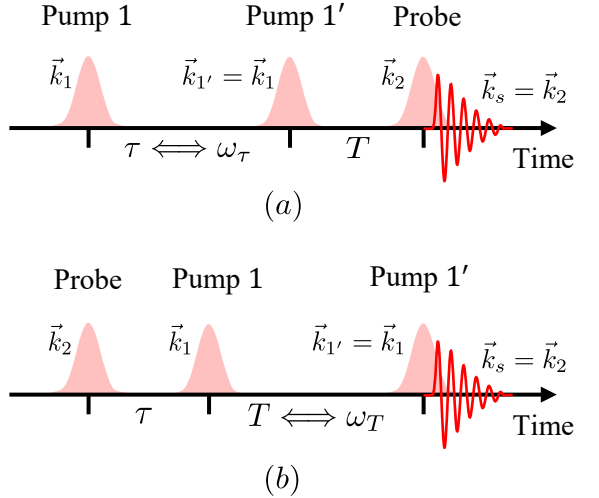


Figure 1. Pulse sequences of third-order (a) 1Q 2D spectroscopy and (b) 2Q 2D spectroscopy under pump-probe geometry. The wave vectors of the two pump pulses are  $\vec{k}_1$  and  $\vec{k}_1'$ , with  $\vec{k}_1' = \vec{k}_1$ , and the the wave vector of the probe pulse is  $\vec{k}_2$ . The probe pulse also serves as the LO, and thus third-order signals with wave vector  $\vec{k}_s = \vec{k}_2$  are self-heterodynely detectable.

consider a general three-level system ( $|g\rangle \leftrightarrow |e\rangle \leftrightarrow |f\rangle$ ). The pathway in Fig. 2(b) corresponds to the traditional pulse sequence of 1Q 2D spectroscopy where the probe pulse arrives lastly, and it suggests that the 2Q signal will emit along  $2\vec{k}_1 - \vec{k}_2$ . Such a direction is non-collinear with the probe pulse that the 2Q signal cannot be self-heterodynely measured. In order to also detect the 2Q signal, the probe pulse is designed to arrive at the sample firstly or secondly [39].

We focus on the pulse sequence with the probe pulse arriving firstly in our current study, and we still denote the intervals between the three pulses as  $\tau$  and  $T$ , as shown in Fig. 1(b). With the probe pulse arriving firstly, the probe pulse and the first pump pulse are used to induce a 2Q coherence  $\rho_{fg}$  during  $T$ , and the conjugated field of the second pump pulse converts the 2Q coherence  $\rho_{fg}$  into a coherence  $\rho_{eg}$  or  $\rho_{fe}$ , as presented by the 2Q pathways ( $R_1$  and  $R_2$ ) in Fig. 2(c) and (d). In these two cases, the 2Q signals have phase matching direction  $\vec{k}_s = \vec{k}_2 + \vec{k}_1 - \vec{k}_1' = \vec{k}_2$ , and thus they are self-heterodynely detectable. However, despite the 2Q signals, 0Q signals with the same phase matching direction will also be measured. We list all detectable 0Q pathways ( $R_3$ ,  $R_4$ , and  $R_5$ ) in Fig. 2(e-g). Unlike in  $R_1$  and  $R_2$  where the conjugated field of the second pump pulse interacts with the sample, in the 0Q pathways, the conjugated field of the first pump pulse contributes. In specific, after the probe pulse inducing a coherence  $\rho_{eg}$ , the conjugated field of the first pump converts  $\rho_{eg}$  into a 0Q coherence  $\rho_{gg}$  or  $\rho_{ee}$  during  $T$ . Then, the second pump pulse induces another coherence  $\rho_{eg}$  or  $\rho_{fe}$ .

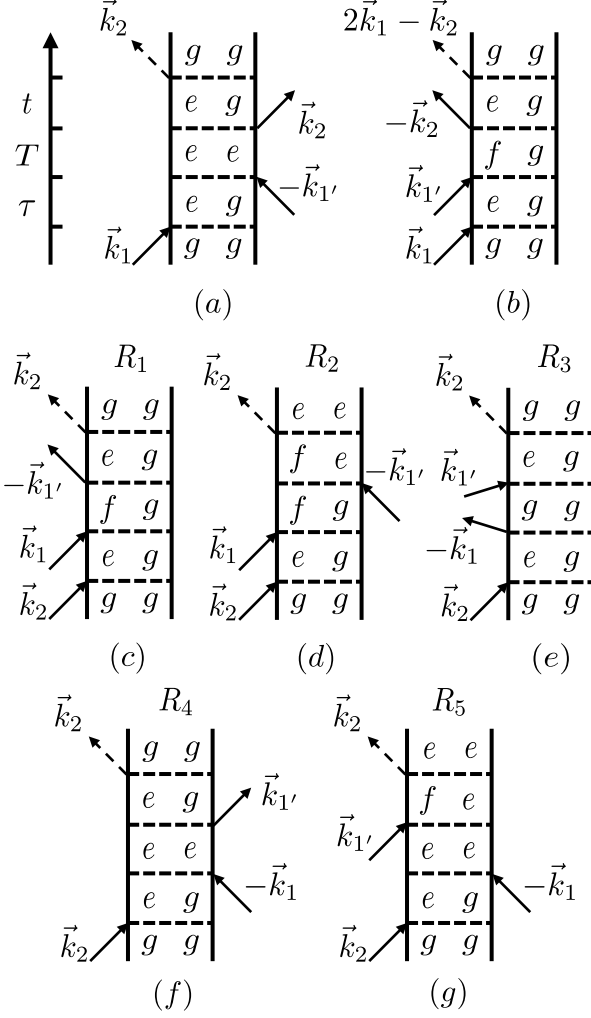


Figure 2. Double-sided Feynman diagrams of (a, b) non-rephasing pathways in 1Q 2D spectroscopy, and (c, d) 2Q and (e-g) 0Q pathways in 2Q 2D spectroscopy under pump-probe geometry. In (a) and (b), the probe pulse interacts with the sample lastly, while in (c) to (g) the probe pulse interacts with the sample firstly.

Additionally for the case with the probe pulse arriving secondly, there are also two 2Q and three 0Q pathways self-heterodynely detectable, which are given in the supplementary material. Note that in 2D spectroscopy experiments under pump-probe geometry, the interval between the pump pulses [13, 32, 41] and the time ordering of the probe pulse are typically controlled independently. Letting the probe pulse arrive secondly (i.e., inserting the probe pulse between the two pump pulse) will mix up the uncertainties of time control methods.

### B. Phase accumulation in heterodyne detection

In the conventional 1Q 2D spectroscopy, the signal field  $E_s(\tau, T, \omega_t)$  induced by the three different pulses is

emitted promptly after the probe pulse, as illustrated in Fig. 1(a). This signal field is contemporaneously detected by the spectrometer alongside the probe pulse (i.e., the LO), and the heterodynely measured signal is expressed as  $S(\tau, T, \omega_t) = 2\text{Re}[E_s(\tau, T, \omega_t)E_{\text{LO}}^*(\omega_t)]$ , where  $E_{\text{LO}}(\omega_t) = E_2(\omega_t)$  is the field of the probe pulse.

However, in the 2Q 2D spectroscopy depicted in Fig. 1(b), the third-order signal is exclusively emitted upon the arrival of the second pump pulse. In such a scenario, the signal field lags behind the probe pulse by an interval  $\tau + T$ , causing the probe pulse to accumulate an additional phase  $\exp[-i\omega_t(\tau + T)]$  through propagation before acting as the LO [28, 39]. Taking into account this phase accumulation, the measured signal is now expressed as

$$S(\tau, T, \omega_t) = 2\text{Re}[E_s(\tau, T, \omega_t)E_2^*(\omega_t)e^{i\omega_t(\tau+T)}], \quad (1)$$

noticing that  $E_{\text{LO}}(\omega_t) = E_2(\omega_t)e^{-i\omega_t(\tau+T)}$  now.

### C. Rotating frame

2D spectrum  $S(\tau, \omega_T, \omega_t)$  is obtained by sampling and Fourier transforming  $S(\tau, T, \omega_t)$  with respect to  $T$ . In order to reduce the sampling rate required to the Nyquist-Shannon sampling theorem, a rotating frame [41] is applied to the first pump pulse to reduce the effective oscillation frequency of the 2Q signal during interval  $T$ . This is experimentally achieved by setting an additional phase factor  $\exp[i\omega_{\text{rf}}T]$  to the first pump pulse using the AOM in the pulse shaper [13, 41]. Here,  $\omega_{\text{rf}}$  is the rotating frame frequency.

For 2Q pathways  $R_1$  and  $R_2$ , the 2Q coherence  $\rho_{fg}$  oscillates with frequency  $\omega_{fg}$  (i.e., the eigenfrequency of  $|f\rangle$ ) during interval  $T$ , leading to an oscillation of the third-order response as

$$R_1(\tau, T, \omega_{eg}) \propto e^{-i\omega_{fg}T}, \quad (2)$$

$$R_2(\tau, T, \omega_{fe}) \propto e^{-i\omega_{fg}T}. \quad (3)$$

Here, we have set  $\omega_t = \omega_{eg}$  (i.e., the eigenfrequency of  $|e\rangle$ ) for pathway  $R_1$ , and  $\omega_t = \omega_{fe}$  for pathway  $R_2$ . Applying the rotating frame phase factor  $\exp[i\omega_{\text{rf}}T]$  to the field of the first pump pulse  $E_1$ , the oscillations of 2Q signal fields are modified as

$$E_{R_1}(\tau, T, \omega_{eg}) \propto R_1 E_1 E_1^* E_2 \propto e^{-i(\omega_{fg} - \omega_{\text{rf}})T}, \quad (4)$$

$$E_{R_2}(\tau, T, \omega_{fe}) \propto R_2 E_1 E_1^* E_2 \propto e^{-i(\omega_{fg} - \omega_{\text{rf}})T}. \quad (5)$$

Furthermore, taking into account the accumulated phase  $\exp[i\omega_t(\tau + T)]$  discussed in Sec. II B, the products of 2Q signal fields and the LO field have oscillations

$$E_{R_1}(\tau, T, \omega_{eg}) E_2^*(\omega_{eg}) e^{i\omega_{eg}(\tau+T)} \propto e^{-i(\omega_{fe} - \omega_{\text{rf}})T}, \quad (6)$$

$$E_{R_2}(\tau, T, \omega_{fe}) E_2^*(\omega_{fe}) e^{i\omega_{fe}(\tau+T)} \propto e^{-i(\omega_{eg} - \omega_{\text{rf}})T}. \quad (7)$$

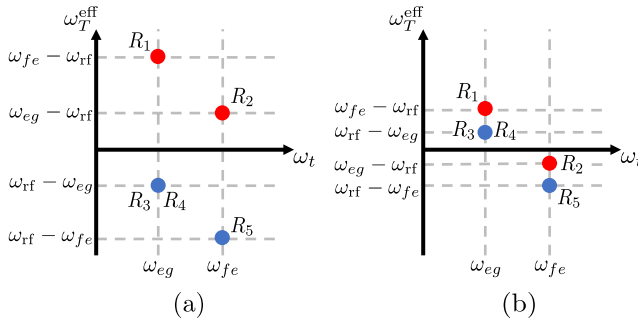


Figure 3. Schematic representation of peak positions for 2Q and 0Q signals. The red dots denote 2Q pathways, and the blue dots denote 0Q pathways. The y axis denotes the effective oscillation frequency  $\omega_T^{\text{eff}}$  during  $T$ . In (a), the rotating frame  $\omega_{\text{rf}}$  is set smaller than both  $\omega_{\text{eg}}$  and  $\omega_{\text{fe}}$ , and 2Q and 0Q pathways occupy the opposite quadrant along the axis of  $\omega_T^{\text{eff}}$ . In (b),  $\omega_{\text{rf}}$  is set between  $\omega_{\text{eg}}$  and  $\omega_{\text{fe}}$ , and 2Q and 0Q pathways could potentially reside at both quadrants.

As a result, 2Q pathways  $R_1$  and  $R_2$  manifest themselves at  $(\omega_{\text{eg}}, \omega_T^{\text{eff}} = \omega_{\text{fe}} - \omega_{\text{rf}})$  and  $(\omega_{\text{fe}}, \omega_T^{\text{eff}} = \omega_{\text{eg}} - \omega_{\text{rf}})$  respectively on 2D spectrum.

The same operation should also be applied to 0Q pathways  $R_3$ ,  $R_4$ , and  $R_5$ . We directly give the results as

$$E_{R_3}(\tau, T, \omega_{\text{eg}}) E_2^*(\omega_{\text{eg}}) e^{i\omega_{\text{eg}}(\tau+T)} \propto e^{-i(\omega_{\text{rf}} - \omega_{\text{eg}})T}, \quad (8)$$

$$E_{R_4}(\tau, T, \omega_{\text{eg}}) E_2^*(\omega_{\text{eg}}) e^{i\omega_{\text{eg}}(\tau+T)} \propto e^{-i(\omega_{\text{rf}} - \omega_{\text{eg}})T}, \quad (9)$$

$$E_{R_5}(\tau, T, \omega_{\text{fe}}) E_2^*(\omega_{\text{fe}}) e^{i\omega_{\text{fe}}(\tau+T)} \propto e^{-i(\omega_{\text{rf}} - \omega_{\text{fe}})T}. \quad (10)$$

Because the phase of  $E_1^*$  is inherited by 0Q signal fields, the rotating frame phase factor is  $\exp[-i\omega_{\text{rf}}T]$  for 0Q pathways. 0Q pathways  $R_3$  and  $R_4$  both generate peaks at  $(\omega_{\text{eg}}, \omega_T^{\text{eff}} = \omega_{\text{rf}} - \omega_{\text{eg}})$ , and the pathway  $R_5$  generates a peak at  $(\omega_{\text{fe}}, \omega_T^{\text{eff}} = \omega_{\text{rf}} - \omega_{\text{fe}})$ . Similar analysis can be performed for all the pathways presented in the supplementary materials.

The setting of the rotating frame determines the signs of effective oscillation frequencies of 2Q and 0Q signals during  $T$ . For instance, if  $\omega_{\text{rf}} < \{\omega_{\text{eg}}, \omega_{\text{fe}}\}$ , 2Q pathways  $R_1$  and  $R_2$  exhibit positive effective oscillation frequencies, whereas 0Q pathways  $R_3$ ,  $R_4$ , and  $R_5$  display negative ones. This situation is illustrated in Fig. 3(a). Conversely, if  $\omega_{\text{rf}} > \{\omega_{\text{eg}}, \omega_{\text{fe}}\}$ , the effective oscillation frequencies of 2Q pathways  $R_1$  and  $R_2$  become negative, while those of 0Q pathways  $R_3$ ,  $R_4$ , and  $R_5$  turn positive. In these two cases, 2Q and 0Q signals can be independently analyzed in opposite quadrants along the axis of  $\omega_T^{\text{eff}}$ . However, when  $\omega_{\text{rf}}$  is set between  $\omega_{\text{eg}}$  and  $\omega_{\text{fe}}$ , both 2Q and 0Q pathways could potentially reside at either quadrants. A depiction of such a situation is provided in Fig. 3(b) where we have assumed that  $\omega_{\text{fe}} > \omega_{\text{eg}}$ . The analogous conclusion hold the same if  $\omega_{\text{fe}} < \omega_{\text{eg}}$ .

Moreover, as presented in Eq. (1), the heterodyne measurement is limited to capturing only the real part of the production of the signal field and the LO field. Following Fourier transformation with respect to time  $T$ , these

real-valued 2Q and 0Q signals exhibit both positive and negative frequency components on the axis of  $\omega_T^{\text{eff}}$ , which further mix up 2Q and 0Q coherences on 2D spectrum. To eliminate the influence of 0Q coherences, we apply techniques of phase cycling and causality enforcement in time  $t$  domain. Detailed explanations of these methods are presented in Sec. III B.

### III. EXTRACTING DOUBLE-QUANTUM COHERENCE

#### A. Phase cycling to remove other contributions

In addition to the third-order 2Q and 0Q signals induced by the three different pulses, the perturbed free induction decay (PFID) [47, 48]  $S_{\text{PFID}}(\tau, T, \omega_t)$  may arise when the sample interacts with the probe pulse once and one of the two pump pulses twice [41]. This undesired signal is also self-heterodyned detected, as it meets the phase matching condition  $\vec{k}_s = \vec{k}_2 \pm \vec{k}_a \mp \vec{k}_a = \vec{k}_2$  (where  $a = 1, 1'$ ).

By applying the technique of phase cycling [5, 41], we can eliminate  $S_{\text{PFID}}(\tau, T, \omega_t)$  from the total signal. Specifically, two experiments with phase arrangements  $(\phi_1 = 0, \phi_{1'} = 0)$  and  $(\phi_1 = 0, \phi_{1'} = \pi)$  are conducted shot-to-shot, where  $\phi_1$  and  $\phi_{1'}$  are correspondingly the relative phases (with respect to the original pump pulse before the pulse shaper) of the first and second pump pulses. The measured signals are then linearly combined through subtraction  $S(\tau, T, \omega_t; \phi_1 = 0, \phi_{1'} = 0) - S(\tau, T, \omega_t; \phi_1 = 0, \phi_{1'} = \pi)$ , in which  $S_{\text{PFID}}(\tau, T, \omega_t)$  is eliminated since  $E_{\text{PFID}}(\tau, T, \omega_t) \propto E_2 |E_a|^2$  is independent of the phases of the two pump pulses. In this subtraction, 2Q and 0Q signals  $S_{R_j}(\tau, T, \omega_t)$  are enhanced because  $E_{R_l}(\tau, T, \omega_t; \phi_1, \phi_{1'}) \propto e^{i(\phi_1 - \phi_{1'})}$  ( $l = 1, 2$ ) for 2Q pathways, and  $E_{R_k}(\tau, T, \omega_t; \phi_1, \phi_{1'}) \propto e^{-i(\phi_1 - \phi_{1'})}$  ( $k = 3, 4, 5$ ) for 0Q pathways.

Moreover, the four-frame cycling scheme  $(\phi_1 = 0, \phi_{1'} = 0)$ ,  $(\phi_1 = 0, \phi_{1'} = \pi)$ ,  $(\phi_1 = \pi, \phi_{1'} = \pi)$ , and  $(\phi_1 = \pi, \phi_{1'} = 0)$  could be applied to further eliminate the influence from the scatter of the pump pulses [3, 41].

#### B. Enforcing causality to extract 2Q signal

By linearly combining the cycled frames in Sec. III A, we cannot distinguish between 2Q and 0Q signals because of the opposite phase dependence between 0Q signal fields  $E_{R_k}(\tau, T, \omega_t; \phi_1, \phi_{1'}) \propto e^{-i(\phi_1 - \phi_{1'})}$  and 2Q signal fields  $E_{R_l}(\tau, T, \omega_t; \phi_1, \phi_{1'}) \propto e^{i(\phi_1 - \phi_{1'})}$ . Such a relation is similar to that between the rephasing and non-rephasing signals in the 1Q 2D spectroscopy [3, 31]. Hence, we can extract 2Q coherence by enforcing causality of the detected signal in time  $t$  domain [3, 31, 39]. The detailed procedure is as follows:

- 1) The third-order signal  $S(\tau, T, \omega_t)$  is detected by a spectrometer in the frequency  $\omega_t$  domain.
- 2)  $S(\tau, T, \omega_t)$  is inversely Fourier transformed with respect to  $\omega_t$  to obtain the time domain signal  $S(\tau, T, t)$ .
- 3) Causality is enforced by assigning the second half of  $S(\tau, T, t)$  with respect to  $t$  to zero, i.e., multiplying  $S(\tau, T, t)$  by the Heaviside step function  $\theta(t)$ ,  $S'(\tau, T, t) = \theta(t)S(\tau, T, t)$ .

After the causality enforcement, the resulting signal  $S'(\tau, T, t)$  becomes complex, with 2Q signals located at  $(\omega_{eg}, \omega_T^{\text{eff}} = \omega_{fe} - \omega_{rf})$  and  $(\omega_{fe}, \omega_T^{\text{eff}} = \omega_{eg} - \omega_{rf})$ , and 0Q signals located at  $(\omega_{eg}, \omega_T^{\text{eff}} = \omega_{rf} - \omega_{eg})$  and  $(\omega_{fe}, \omega_T^{\text{eff}} = \omega_{rf} - \omega_{fe})$ , as shown in Fig. 3.

To complete the extraction, we apply the phase cycling scheme  $(\phi_1 = 0, \phi_1' = 0)$  and  $(\phi_1 = 0, \phi_1' = \pi/2)$  to separate 2Q and 0Q signals with the relations

$$S_{2Q}^{\text{sep}}(\tau, T, t) = S'(\tau, T, t; 0, 0) - iS'(\tau, T, t; 0, \pi/2), \quad (11a)$$

$$S_{0Q}^{\text{sep}}(\tau, T, t) = S'(\tau, T, t; 0, 0) + iS'(\tau, T, t; 0, \pi/2). \quad (11b)$$

This separation is conducted to avoid the possibility that 2Q and 0Q signals reside at both quadrants along the axis of  $\omega_T^{\text{eff}}$  on the 2D spectrum, which is presented in Fig. 3(b).

### C. Frequency shift retrieval

With the time domain signals in Eq. (11), 2Q and 0Q 2D spectra are obtained by Fourier transforming  $S_{2Q}^{\text{sep}}(\tau, T, t)$  and  $S_{0Q}^{\text{sep}}(\tau, T, t)$  with respect to  $T$  and  $t$ . However, due to the phase accumulation represented by  $\exp[i\omega_t(\tau + T)]$  and the rotating frame  $\exp[\pm i\omega_{rf}T]$ , 2Q and 0Q signals in Eq. (11) are actually frequency modulated, which has been described in detail in Sec. II C. Authentic spectra are obtained once the frequencies shifts are retrieved.

In order to compensate the shifts, we firstly Fourier transform the 2Q and 0Q signals in Eq. (11) respect to both  $T$  and  $t$  to derive  $S_{2Q}^{\text{sep}}(\tau, \omega_T^{\text{eff}}, \omega_t)$  and  $S_{0Q}^{\text{sep}}(\tau, \omega_T^{\text{eff}}, \omega_t)$  respectively. Then the frequency values on the axis of  $\omega_T^{\text{eff}}$  for  $S_{2Q}^{\text{sep}}(\tau, \omega_T^{\text{eff}}, \omega_t)$  are all added by  $\omega_t + \omega_{rf}$  to obtain the frequency shift retrieved 2Q 2D spectra  $S_{2Q}^{\text{rtrv}}(\tau, \omega_T, \omega_t)$ . This operation shift the effective oscillation frequencies during  $T$  back to the authentic values. Similarly, the frequency values on the axis of  $\omega_T^{\text{eff}}$  for  $S_{0Q}^{\text{sep}}(\tau, \omega_T^{\text{eff}}, \omega_t)$  are all added by  $\omega_t - \omega_{rf}$  to obtain the frequency shift retrieved 0Q 2D spectra  $S_{0Q}^{\text{rtrv}}(\tau, \omega_T, \omega_t)$ . Finally, these two frequency-shift-retrieved spectra should be multiplied by an additional phase factor  $\exp[i\omega_t\tau]$  to compensate the phase accumulation of the probe pulse during  $\tau$ .

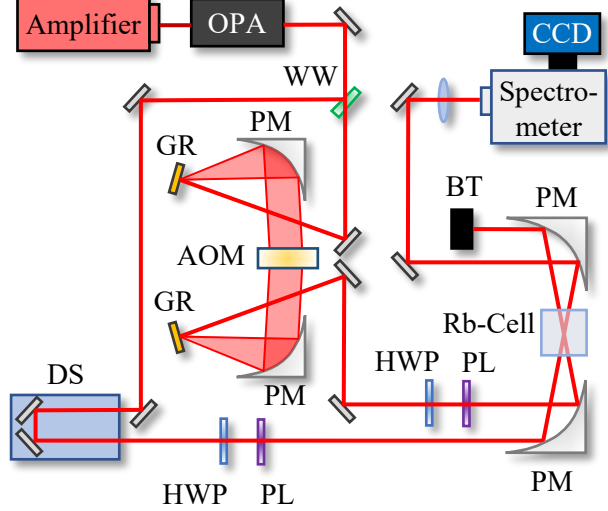


Figure 4. The experimental setup of the 2Q 2DES under pump-probe geometry. This setup is identical with the typical 1Q 2DES, whereas the difference is the pulse sequence, as presented in Fig. 1. Amplifier: Ti:Sapphire amplifier laser system; OPA: optical parametric amplifier; WW: wedged window; PM: parabolic mirror; GR: optical grating; AOM: acousto-optic modulator; DS: delay stage; HWP: half-wave plate; PL: polarizer; BT: beam trap; CCD: charge coupled device camera. The sample is a rubidium ( $^{87}\text{Rb}$ ) vapor cell containing a 450 torr Nitrogen buffer gas. The cell is heated at 120 °C during measurement.

## IV. EXPERIMENT DEMONSTRATION

In this section, we demonstrate the detection and extraction scheme of the 2Q electronic coherence in experiment with rubidium atoms ( $^{87}\text{Rb}$ ) using the 2Q 2DES.

### A. Experimental setup

The experiment setup is presented in Fig. 4. A Ti:Sapphire amplifier laser system generates laser pulses (800 nm, 30.8 fs) at a 1 kHz repetition rate. The central wavelength of the laser pulses is shifted using an optical parametric amplifier (OPA). The laser beam after the OPA is divided by a wedged window into the pump and the probe beams. A pulse shaper consisting of an AOM, two parabolic mirrors, and two gratings with 4-f geometry converts one pump pulse into two pump pulses with interval  $T$ . The interval  $\tau$  between the probe and the first pump pulse is controlled by a delay stage on the probe arm. The pump and the probe beams are focused onto the sample (a  $^{87}\text{Rb}$  vapor cell) using a parabolic mirror. After the sample, the spectrum of the probe pulse is detected by a charge coupled device (CCD) camera connected to a spectrometer. Note that the polarizations of

the pump and probe pulses are set horizontal with half-wave plates and polarizers before hitting the sample. In addition,  $\tau$  is kept zero in our experiment.

The vapor cell is a cube with an edge length of 15 mm. During the measurement, the cell is heated at 120 °C with corresponding atomic density of around  $1.65 \times 10^{13} \text{ cm}^{-3}$  of  $^{87}\text{Rb}$  atoms [49]. In addition, the cell contains a 450 torr Nitrogen buffer gas which broadens the resonance linewidths of  $^{87}\text{Rb}$  through collision.

The wavelength of the output pulses from the OPA centers at 783 nm which adjoins the  $D_2$  transition ( $5^2S_{1/2} \rightarrow 5^2P_{3/2}$ ) frequency of  $2\pi \times 384.2 \text{ THz}$  (780 nm) of  $^{87}\text{Rb}$  atoms [49]. The pulse spectrum has a bandwidth (FWHM) of 24 nm, meaning that not only the  $D_2$  transition, but also the  $D_1$  transition ( $5^2S_{1/2} \rightarrow 5^2P_{1/2}$ ) at a frequency of  $2\pi \times 377.1 \text{ THz}$  (795 nm) and the excited states transition ( $5^2P_{3/2} \rightarrow 5^2D$ ) at a frequency of  $2\pi \times 386.3 \text{ THz}$  (776 nm) could be simultaneously induced.

## B. Experimental results

To demonstrate the extraction of 2Q coherence, we utilize a phase cycling scheme ( $\phi_1 = 0, \phi_1' = 0$ ), ( $\phi_1 = 0, \phi_1' = \pi/2$ ), ( $\phi_1 = 0, \phi_1' = \pi$ ), and ( $\phi_1 = 0, \phi_1' = 3\pi/2$ ), and the corresponding spectra (denoted as  $S_1$ ,  $S_2$ ,  $S_3$ , and  $S_4$ ) are detected shot-to-shot. These spectra are combined by subtractions to generate two spectra  $S(0, T, \omega_t; 0, 0) = S_1(0, T, \omega_t) - S_3(0, T, \omega_t)$  and  $S(0, T, \omega_t; 0, \pi/2) = S_2(0, T, \omega_t) - S_4(0, T, \omega_t)$  which correspond to spectra in cycling scheme ( $\phi_1 = 0, \phi_1' = 0$ ) and ( $\phi_1 = 0, \phi_1' = \pi/2$ ) with the PFID signal eliminated. The rotating frame is set at 787 nm, corresponding to a frequency of  $\omega_{\text{rf}}/2\pi = 380.9 \text{ THz}$ , and  $T$  is scanned from 0 to 14.4 ps with a step size of 80 fs.

By applying the separation process in Sec. III B, we obtain the separated 2Q and 0Q 2D spectra without frequency shifts retrieved,  $S_{2\text{Q}}^{\text{sep}}(\tau, \omega_T^{\text{eff}}, \omega_t)$  and  $S_{0\text{Q}}^{\text{sep}}(\tau, \omega_T^{\text{eff}}, \omega_t)$ , as illustrated in Fig. 5(a) and (b). Subsequently, the y axes of these two spectra are added by  $\omega_t + \omega_{\text{rf}}$  and  $\omega_t - \omega_{\text{rf}}$ , respectively, resulting in the authentic 2Q and 0Q 2D spectra,  $S_{2\text{Q}}^{\text{triv}}(\tau, \omega_T, \omega_t)$  and  $S_{0\text{Q}}^{\text{triv}}(\tau, \omega_T, \omega_t)$ , as shown in Fig. 5(c) and (d). Note that we additionally calibrate the axis of  $\omega_T$  of the 2Q 2D spectrum by adding  $2\pi \times 0.3 \text{ THz}$  to have the two highest peaks settled at  $\omega_T/2\pi = 770.5 \text{ THz}$  [34] in Fig. 5(c), where the highest horizontal dashed line denotes the frequency of 770.5 THz. Such operation is performed to compensate the shift in the calibration of nonlinearities (typically in the AOM) in the system.

After the frequency calibration, the 2Q and 0Q 2D spectra of  $^{87}\text{Rb}$  in Fig. 5(c) and (d) show identical peak locations as those have been reported in other systems utilizing either BOXCARS or collinear geometries [34, 42]. Specifically, in Fig. 5(c) the two peaks aligned on the highest horizontal dashed line corresponds to the doubly excited level of an individual  $^{87}\text{Rb}$  atom. The three lower horizontal dashed lines correspond to

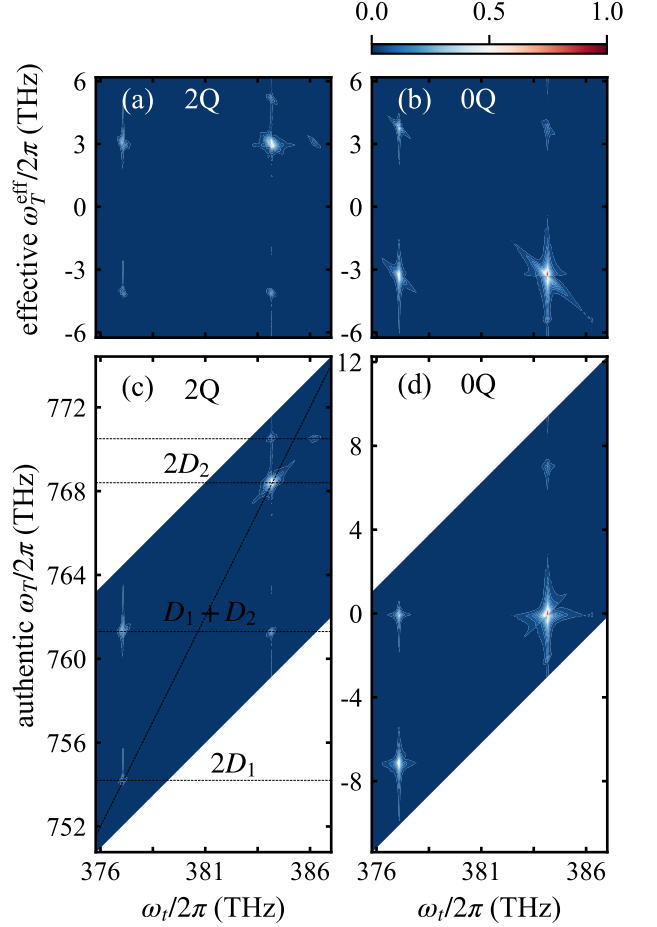


Figure 5. 2Q 2D absolute spectra and 0Q 2D absolute spectra of  $^{87}\text{Rb}$ . (a) and (b) are 2Q and 0Q 2D spectra without frequency shifts retrieved, and their y axes represent the effective frequency  $\omega_T^{\text{eff}}$ . (c) and (d) are obtained by retrieving frequency shifts of (a) and (b), with their y axes representing the authentic frequency  $\omega_T$ . In (c), the peaks on the highest horizontal dashed line corresponds to the doubly excited level of an individual  $^{87}\text{Rb}$  atom, i.e.,  $5^2D$ . The peaks on the other (lower) three horizontal dashed lines correspond to the doubly excited levels originated from dipole-dipole interactions.

frequencies 754.2 THz, 761.3 THz, and 768.4 THz, respectively, signifying the collective resonances originated from dipole-dipole interactions of  $D_1 + D_1$ ,  $D_1 + D_2$ , and  $D_2 + D_2$  transitions of two  $^{87}\text{Rb}$  atoms. In Fig. 5(d), two peaks on  $\omega_T = 0$  are contributed by population states during  $T$ , and the other two peaks on  $\omega_T = \pm 7.1 \text{ THz}$  correspond to coherences between  $D_1$  and  $D_2$  transitions. The detailed double-sided Feynman diagrams of all the corresponding pathways are listed in the supplementary material. We note that we have firstly accomplished the simultaneous observation of doubly excited level of an individual  $^{87}\text{Rb}$  atom and collective resonances arising from dipole-dipole interactions of both  $D_1$  and  $D_2$  transitions [42] within a shared 2Q 2D spectrum.

## V. CONCLUSION

2D spectroscopy under pump-probe geometry is an approach alleviating the challenges of implementing 2D spectroscopy, and has achieved considerable success in 1Q 2D spectroscopy since its invention. However, in the realm of the third-order 2Q studies using 2D spectroscopy, the pump-probe geometry has been limited due to its phase matching direction, while other geometries, such as the BOXCARS and collinear geometries, have historically taken precedence. This situation was only recently broken by Farrell and Zanni [39] with a permuted-pump-probe pulse sequence in 2D IR spectroscopy. Our work extends the application of this method to 2Q 2DES, providing an alternative for investigating electronic 2Q coherence through 2D spectroscopy.

In our 2Q 2DES under pump-probe geometry, the probe pulse arrives firstly at the sample followed by the two pump pulses. In such a pulse sequence, not only the 2Q but also the 0Q coherences are detected due to their same phase matching direction. We have discussed in detail the effective oscillation frequencies of 2Q and 0Q coherences during  $T$ . We present that both 2Q and 0Q coherences may appear at either quadrants along the axis of  $\omega_f^{\text{eff}}$  on the 2D spectrum. Thus, we separate the 2Q and 0Q coherence onto two distinct spectra by using

the technique of causality enforcement and by applying the typical phase cycling scheme ( $\phi_1 = 0, \phi_1' = 0$ ) and ( $\phi_1 = 0, \phi_1' = \pi/2$ ) of the two pump pulses. 2Q and 0Q spectra are then analyzed without disturbing each other.

## Conflict of Interest Statement

The authors have no conflicts to disclose.

## Author Contributions

Mao-Rui Cai: Conceptualization (equal); Data Curation (lead); Formal Analysis (equal); Methodology (equal); Software (equal); Writing-original draft (lead); Writing-review & editing (supporting). Xue Zhang: Formal Analysis (equal); Methodology (equal); Writing-review & editing (supporting). Zi-Qian Cheng: Formal Analysis (equal); Writing-review & editing (supporting). Teng-Fei Yan: Software (equal); Writing-review & editing (supporting). Hui Dong: Conceptualization (equal); Formal Analysis (equal); Funding acquisition (lead); Methodology (equal); Supervision (lead); Project Administration (lead); Writing-review & editing (lead).

---

[1] S. Mukamel, *Principles of Nonlinear Optical Spectroscopy* (Oxford University Press, 1995).

[2] M. Cho, *Two-Dimensional Optical Spectroscopy* (CRC Press, 2009).

[3] P. Hamm and M. Zanni, *Concepts and Methods of 2D Infrared Spectroscopy* (Cambridge University Press, 2011).

[4] D. M. Jonas, *Annual Review of Physical Chemistry* **54**, 425 (2003).

[5] P. Tian, D. Keusters, Y. Suzuki, and W. S. Warren, *Science* **300**, 1553 (2003).

[6] X. Dai, M. Richter, H. Li, A. D. Bristow, C. Falvo, S. Mukamel, and S. T. Cundiff, *Phys. Rev. Lett.* **108**, 193201 (2012).

[7] B. Lomsadze and S. T. Cundiff, *Science* **357**, 1389 (2017).

[8] Y. Zhang, J. Shi, X. Li, S. L. Coy, R. W. Field, and K. A. Nelson, *Proceedings of the National Academy of Sciences* **118**, e2020941118 (2021).

[9] G. S. Schlau-Cohen, A. Ishizaki, and G. R. Fleming, *Chemical Physics* **386**, 1 (2011).

[10] T. Elsaesser, *Accounts of Chemical Research* **42**, 1220 (2009).

[11] M. C. Asplund, M. T. Zanni, and R. M. Hochstrasser, *Proceedings of the National Academy of Sciences* **97**, 8219 (2000).

[12] N. Demirdöven, M. Khalil, and A. Tokmakoff, *Phys. Rev. Lett.* **89**, 237401 (2002).

[13] C. T. Middleton, A. M. Woys, S. S. Mukherjee, and M. T. Zanni, *Methods* **52**, 12 (2010).

[14] C. T. Middleton, P. Marek, P. Cao, C.-c. Chiu, S. Singh, A. M. Woys, J. J. de Pablo, D. P. Raleigh, and M. T. Zanni, *Nature Chemistry* **4**, 355 (2012).

[15] M. Cowan, J. Ogilvie, and R. Miller, *Chemical Physics Letters* **386**, 184 (2004).

[16] T. Brixner, J. Stenger, H. M. Vaswani, M. Cho, R. E. Blankenship, and G. R. Fleming, *Nature* **434**, 625 (2005).

[17] N. H. C. Lewis, N. L. Gruenke, T. A. A. Oliver, M. Ballottari, R. Bassi, and G. R. Fleming, *The Journal of Physical Chemistry Letters* **7**, 4197 (2016).

[18] C. hung Tseng, S. Matsika, and T. C. Weinacht, *Opt. Express* **17**, 18788 (2009).

[19] B. A. West and A. M. Moran, *The Journal of Physical Chemistry Letters* **3**, 2575 (2012).

[20] J. Lu, Y. Zhang, H. Y. Hwang, B. K. Ofori-Okai, S. Fleischer, and K. A. Nelson, *Proceedings of the National Academy of Sciences* **113**, 11800 (2016).

[21] K. Reimann, M. Woerner, and T. Elsaesser, *The Journal of Chemical Physics* **154** (2021).

[22] T. A. A. Oliver, N. H. C. Lewis, and G. R. Fleming, *Proceedings of the National Academy of Sciences* **111**, 10061 (2014).

[23] H. Dong, N. H. C. Lewis, T. A. A. Oliver, and G. R. Fleming, *The Journal of Chemical Physics* **142**, 174201 (2015).

[24] N. H. C. Lewis, H. Dong, T. A. A. Oliver, and G. R. Fleming, *The Journal of Chemical Physics* **142**, 174202 (2015).

[25] T. L. Courtney, Z. W. Fox, K. M. Slenkamp, and M. Khalil, *The Journal of Chemical Physics* **143**, 154201 (2015).

[26] S. T. Cundiff and S. Mukamel, *Physics Today* **66**, 44 (2013).

[27] J. Kim, S. Mukamel, and G. D. Scholes, *Accounts of Chemical Research* **42**, 1375 (2009).

[28] T. Brixner, T. Mančal, I. V. Stiopkin, and G. R. Fleming, *The Journal of Chemical Physics* **121**, 4221 (2004).

[29] K. W. Stone, K. Gundogdu, D. B. Turner, X. Li, S. T. Cundiff, and K. A. Nelson, *Science* **324**, 1169 (2009).

[30] E. M. Grumstrup, S.-H. Shim, M. A. Montgomery, N. H. Damrauer, and M. T. Zanni, *Opt. Express* **15**, 16681 (2007).

[31] J. A. Myers, K. L. M. Lewis, P. F. Tekavec, and J. P. Ogilvie, *Opt. Express* **16**, 17420 (2008).

[32] D. Brida, C. Manzoni, and G. Cerullo, *Opt. Lett.* **37**, 3027 (2012).

[33] W. Rock, Y.-L. Li, P. Pagano, and C. M. Cheatum, *The Journal of Physical Chemistry A* **117**, 6073 (2013).

[34] F. Gao, S. T. Cundiff, and H. Li, *Opt. Lett.* **41**, 2954 (2016).

[35] S. Yu, Y. Geng, D. Liang, H. Li, and X. Liu, *Opt. Lett.* **47**, 997 (2022).

[36] D. B. Turner and K. A. Nelson, *Nature* **466**, 1089 (2010).

[37] S. Yu, M. Titze, Y. Zhu, X. Liu, and H. Li, *Opt. Lett.* **44**, 2795 (2019).

[38] P. Brosseau, S. Palato, H. Seiler, H. Baker, and P. Kambhampati, *The Journal of Chemical Physics* **153**, 234703 (2020).

[39] K. M. Farrell and M. T. Zanni, *The Journal of Chemical Physics* **157**, 014203 (2022).

[40] Z. T. Armstrong, K. M. Forlano, C. R. Roy, M. Bohlmann Kunz, K. Farrell, D. Pan, J. C. Wright, S. Jin, and M. T. Zanni, *Journal of the American Chemical Society* **145**, 18568 (2023).

[41] S.-H. Shim and M. T. Zanni, *Phys. Chem. Chem. Phys.* **11**, 748 (2009).

[42] J. Yan, S. Revesz, D. Liang, and H. Li, *Phys. Rev. A* **105**, 052810 (2022).

[43] J. A. Myers, K. L. M. Lewis, F. D. Fuller, P. F. Tekavec, C. F. Yocom, and J. P. Ogilvie, *The Journal of Physical Chemistry Letters* **1**, 2774 (2010).

[44] M. Thämer, L. D. Marco, K. Ramasesha, A. Mandal, and A. Tokmakoff, *Science* **350**, 78 (2015).

[45] B. Xiang, R. F. Ribeiro, M. Du, L. Chen, Z. Yang, J. Wang, J. Yuen-Zhou, and W. Xiong, *Science* **368**, 665 (2020).

[46] Y. Song, R. Sechrist, H. H. Nguyen, W. Johnson, D. Abramavicius, K. E. Redding, and J. P. Ogilvie, *Nature Communications* **12**, 2801 (2021).

[47] P. Hamm, *Chemical Physics* **200**, 415 (1995).

[48] P. Brosseau, H. Seiler, S. Palato, C. Sonnichsen, H. Baker, E. Socie, D. Strandell, and P. Kambhampati, *The Journal of Chemical Physics* **158**, 084201 (2023).

[49] D. A. Steck, “Rubidium 87 d line data,” <http://steck.us/alkalidata>.